



## Performance degradation in proton-conducting ceramic fuel cell and electrolyzer stacks

Long Q. Le <sup>a,\*</sup>, Charlie Meisel <sup>b</sup>, Carolina H. Hernandez <sup>a</sup>, Jake Huang <sup>b</sup>, Youdong Kim <sup>b</sup>, Ryan O'Hare <sup>b</sup>, Neal P. Sullivan <sup>a</sup>

<sup>a</sup> Mechanical Engineering Department, Colorado Fuel Cell Center, Colorado School of Mines, Golden, CO 80401, USA

<sup>b</sup> Metallurgical and Materials Engineering Department, Colorado Center for Advanced Ceramics, Colorado School of Mines, Golden, CO 80401, USA

### HIGHLIGHTS

- Stability of proton-conducting ceramic fuel-cell and electrolyzer is investigated.
- Modification of the air-steam electrode greatly improved the cell stability.
- Degradation rates of less than 1%  $\text{khr}^{-1}$  have been demonstrated.

### ARTICLE INFO

#### Keywords:

Proton-conducting ceramic  
Degradation  
Fuel cell  
SOFC  
Electrolysis

### ABSTRACT

Proton-conducting ceramics are emerging as enabling materials for efficient electrochemical electricity generation, energy storage, and fuels synthesis. In this work, we present longer-term degradation results for protonic-ceramic fuel cells and electrolyzers based on a  $\text{BaCe}_{0.4}\text{Zr}_{0.4}\text{Y}_{0.1}\text{Yb}_{0.1}\text{O}_{3-\delta}$  (BCZYYb) electrolyte. The cells are packaged within unit-cell stacks, including metallic interconnects, current collectors, sealing glasses and gaskets. Durability is found to be superior in protonic-ceramic electrolyzers in comparison to fuel cells. Operating conditions have a large impact on degradation rates; better stability is found at fuel-cell operating temperatures above 600 °C, and electrolyzer steam feeds below 20 %. We find that both fuel-cell and electrolyzer degradation is greatly reduced via the introduction of a gadolinium-doped ceria interlayer between the electrolyte and the air-steam electrode. Fuel-cell degradation falls to 1.2%  $\text{khr}^{-1}$  under methane fuel at 600 °C; electrolyzer degradation is reduced to 1%  $\text{khr}^{-1}$  at 550 °C and 50% steam. Further analyses of electrochemical impedance spectroscopy and distribution of relaxation times provide insight to root processes and degradation phenomena in protonic electroceramics.

### 1. Introduction

Proton-conducting ceramics present an emerging class of electrochemical materials that are now being harnessed to address societal challenges in electricity generation, energy storage, and “green” chemical synthesis, including hydrogen [1,2], benzene [3], methane [4], and ammonia [5] production. Unlike more well-established oxygen-ion-conducting electroceramics such as yttria-stabilized zirconia (YSZ) or gadolinium-doped ceria (GDC), protonic ceramics primarily transport  $\text{H}^+$  through the dense electrolyte. This feature greatly reduces the impacts of concentration polarization at the fuel electrode, increasing protonic-ceramic fuel-cell performance and efficiency. Similarly, protonic ceramics have the potential to produce pure, dry  $\text{H}_2$  during  $\text{H}_2\text{O}$  electrolysis, simplifying downstream hydrogen processing and purification.

Fig. 1 illustrates salient aspects of a planar protonic-ceramic electrolysis cell (PCEC); the cell design draws from previously established architectures reminiscent of oxygen-ion-conducting solid-oxide fuel cells and electrolyzers (SOFCs and SOECs). As illustrated, a four-layer, protonic-ceramic membrane-electrode assembly (MEA) is packaged between two metallic interconnects. An external power supply drives electric current across the interconnects into the cell to facilitate the  $\text{H}_2\text{O}$ -electrolysis process. Steam enters through the upper channel and high-purity hydrogen leaves via the lower channel. While Fig. 1 presents an electrolysis cell, protonic ceramics can also operate in fuel-cell mode (PCFC) to efficiently convert the chemical energy of fuels into electricity. Stable, reversible operation has also been demonstrated [1, 6].

\* Corresponding author.

E-mail address: [long.le@pnnl.gov](mailto:long.le@pnnl.gov) (L.Q. Le).

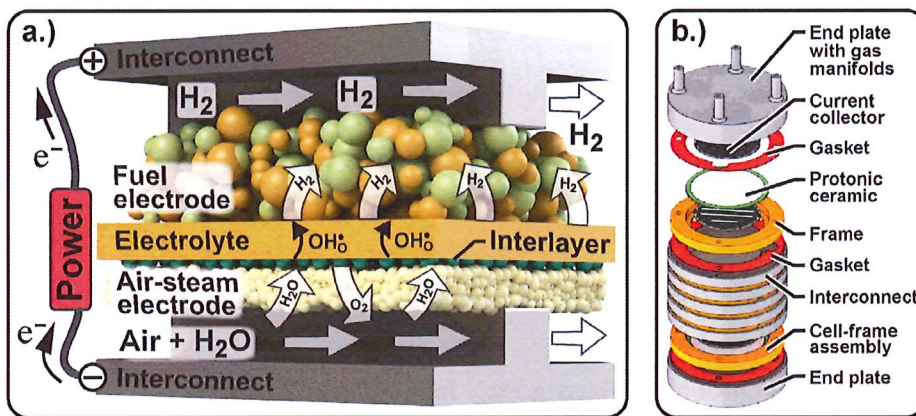


Fig. 1. (a) Illustration of planar proton-conducting ceramic electrolysis cell; and (b) electrolyzer stack schematic.  
Source: Used with permission [7].

The protonic-ceramic electrolyte is a ~10  $\mu\text{m}$ -thick mixed ionic-electronic conducting (MIEC) perovskite material. Many perovskite compositions and stoichiometries are possible; we have found yttrium-ytterbium-doped barium cerate-zirconate  $\text{BaCe}_{0.4}\text{Zr}_{0.4}\text{Y}_{0.1}\text{Yb}_{0.1}\text{O}_{3-\delta}$  (BCZYYb4411 or BCZYYb) to demonstrate the most-encouraging blend of durability and performance [7].

As in many  $\text{O}^{2-}$ -ion-conducting solid-oxide devices, the protonic-ceramic fuel electrode is a relatively thick (~0.8 mm), porous ceramic-metallic composite (cermet) composed of Ni and the electrolyte material (BCZYYb). Nickel serves as the electronic conductor, while BCZYYb is the proton conductor. In addition to its electrochemical function, the fuel electrode also serves as the cell structural support. The air-steam electrode is a porous electro-ceramic material typically a few tens-of-microns thick; we have observed strong performance using  $\text{BaCo}_{0.4}\text{Fe}_{0.4}\text{Zr}_{0.1}\text{Y}_{0.1}\text{O}_{3-\delta}$  (BCFZY). BCFZY is a triple-conducting oxide that transports protons, oxygen ions, and electrons, and is stable in the oxidizing environment present at the steam electrode. We have found improvements in cell durability through application of a thin interlayer of 10 mol-% gadolinium-doped ceria placed between the air-steam electrode and the electrolyte [7].

Protonic-ceramic devices bring several key benefits and advantages over state-of-the-art PEM or solid-oxide technologies for achieving cost and performance targets:

- Protonic-ceramic electrolyzers can produce pure, dry, H<sub>2</sub>, potentially at elevated pressure, substantially reducing green-H<sub>2</sub> system complexity and operational cost;
- Protonic-ceramic fuel cells are less susceptible to concentration polarization, as product H<sub>2</sub>O is produced at the air-steam electrode, while the fuel electrode maintains high H<sub>2</sub> partial pressure;
- The small size of protons transported through the BCZYYb electrolyte results in higher ionic conductivity in comparison to state-of-the-art  $\text{O}^{2-}$ -ion-conducting devices; this, in turn, enables efficient device operation at temperatures that are generally 200–300 °C lower than that of SOFCs and SOECs;
- The ~500 °C PCEC operating temperature, while lower than that of  $\text{O}^{2-}$  ion-conductors, is much higher than that of PEM electrolyzers, enabling higher thermodynamic efficiency that promotes lower-cost green-H<sub>2</sub> production;
- Intermediate-temperature operation (400–600 °C) reduces stack and balance-of-plant materials requirements [7], mitigates thermally driven degradation processes, improves thermal-cycling tolerance, and enables more-flexible thermal integration.

The technology readiness level (TRL) of protonic ceramics is perhaps three (3) [8], with the great majority of protonic-ceramics reports focusing on materials-based, single-cell studies. These authors have found

only a single report of protonic-ceramic stacks in the archival literature [7], illustrating the relatively early stage of the technology. That said, protonic ceramics are witnessing significant research investment, with promising model predictions of system-level efficiency [9].

Scale-up of protonic ceramics beyond the button cell brings many questions. How does lower-temperature operation impact fuel-cell and electrolyzer degradation rates? How is degradation impacted by fuel-cell and electrolyzer operating conditions? What are the fundamental mechanisms of degradation in protonic ceramic MEAs and stacks? Here, through a series of longer-duration experiments on protonic-ceramic membrane-electrode assemblies and stacks, we seek to provide insight on these pressing issues facing this emerging technology.

Degradation in oxygen-ion conducting solid-oxide devices has witnessed extensive study, providing useful context for protonic ceramic devices. Nickel agglomeration in the fuel electrode has proven problematic for both SOFCs and SOECs. The resulting increase in particle size brings a decrease in triple-phase boundary (TPB) length, reducing performance [10].

Solid-oxide electrolysis cells similarly suffer from nickel segregation and depletion away from the TPB's. This segregation is promoted by the high H<sub>2</sub>O concentration at the fuel electrode, leading to formation of highly mobile  $\text{Ni(OH)}_2$  and migration of nickel away from the electrode-electrolyte interface [11].

Carbon-containing fuels can lead to solid-carbon formation within the SOFC fuel electrode. Coking risk is dependent upon temperature and gas composition, particularly steam-to-carbon ratio. Carbon formation can coat the nickel phase to drastically reduce catalytic activity. Further coking can lead to cell fracture and catastrophic failure [12,13].

Degradation at the solid-oxide air-steam electrode often involves interdiffusion of cations, microstructure coarsening, and formation of secondary phases. Lanthanum-based air-steam electrodes exhibit poor stability in high-CO<sub>2</sub>, high-H<sub>2</sub>O environments that can bring SrCO<sub>3</sub> formation, especially at lower temperatures (~600 °C). The most-common factors observed in H<sub>2</sub>O-promoted degradation in solid-oxide devices include degree of humidification, applied current density, and operating temperature [14]. Adsorption of H<sub>2</sub>O induces Sr-segregation and Mn<sub>3</sub>O<sub>4</sub> generation at the electrode surfaces. La<sub>2</sub>Zr<sub>2</sub>O<sub>7</sub> and Mn<sub>2</sub>O<sub>3</sub>-formation reduces conductivity at LSM-YSZ interfaces [15]. LSCF electrodes can suffer from volatile Sr(OH)<sub>2</sub> formation, bringing Sr-depletion.

Stack packaging and balance-of-plant components can also promote cell-level degradation. Chromium contamination from Cr-containing metallic interconnects is of particular concern. Volatile CrO<sub>3</sub> and CrO<sub>2</sub>(OH)<sub>2</sub> species formed in the interconnect scale can transport and deposit within the air-steam electrode. The Cr-poisoning rate is dependent upon the operating temperature and humidity. Dense Cr<sub>2</sub>O<sub>3</sub> layers

form preferentially at LSM electrode–electrolyte interfaces, while LSC-LSCF electrodes are fouled through a more-uniform distribution of chromium distributed throughout the electrode [16].

Membrane–electrode assemblies are commonly bonded and sealed to stack components using glass-ceramic sealants that can contain significant silica, alumina, and sodium phases. Like chromia, these materials can volatilize and deposit at critical cell-level interfaces [16]. Jiang et al. [17] found that these materials can lead to coarsening of LSM-based air–steam electrodes.

With far-different materials sets, lower operating temperatures, and fundamentally different operating principles, long-term performance degradation in proton-conducting ceramic devices is almost certain to differ substantially from that of oxygen-ion-conducting electroceramics. While the literature has few reports of longer-term performance in protonic ceramics, encouraging preliminary results have been demonstrated at the button-scale. Duan et al. [18] has shown strong carbon and sulfur tolerance for thousands of hours in hydrocarbon-fueled PCFC button cells. The highly basic surface chemistry of the Ba-based perovskite, combined with ex-solution of Ni-nanoparticles, are postulated to bring the superior carbon and sulfur tolerance. PCFC-stacks have also shown long-term stability, demonstrating degradation below 1.5%/1000 hr over 2500 hr of continuous operation at 550 °C [7].

In this paper, we expand on these degradation studies to further explore the protonic-ceramics operational space in larger area ( $\sim 5 \text{ cm}^2$  active area) devices in a unit-cell stack environment, including metallic interconnects, current collectors, sealing glasses and gaskets. This study includes both fuel cell and electrolysis operation, and the role of both temperature and steam concentration on protonic-ceramic device degradation.

## 2. Materials and methods

Our degradation studies utilize planar, electrode-supported devices following the materials and fabrication processes detailed in Le et al. [7]. Membrane–electrode assemblies feature 40 mm-dia cells that are packaged into unit- and multi-cell stacks. Membrane–electrode assembly (MEA) materials are centered on a  $\text{BaCe}_{0.4}\text{Zr}_{0.4}\text{Y}_{0.1}\text{Yb}_{0.1}\text{O}_{3-\delta}$  (BCZYYb) electrolyte, for which we previously reported encouraging performance and stability [7]. The electrode-supported architecture and fabrication process draws heavily from that of planar MEAs utilized in  $\text{O}_2^-$ -ion-conducting solid-oxide devices.

### 2.1. Fuel electrode fabrication process

The fuel electrode is a porous ceramic–metallic “cermet” composite combining an electron-conducting nickel phase with a proton-conducting ceramic phase. The BCZYYb ceramic phase is prepared by first mixing stoichiometric ratios of  $\text{BaCO}_3$  (Alfa Aesar 14341),  $\text{CeO}_2$  (Alfa Aesar 11328),  $\text{ZrO}_2$  (Sigma Aldrich 230693),  $\text{Y}_2\text{O}_3$  (Alfa Aesar 11182),  $\text{Yb}_2\text{O}_3$  (Alfa Aesar 36252). These precursors are then mixed with  $\text{NiO}$  (Alfa Aesar 45094) and potato starch (Alfa Aesar A11961) in a mass ratio of 60 wt-%  $\text{NiO}$  : 40 wt-% BCZYYb + 20 wt-% starch. This mixture is ball-milled in isopropanol for 72 h, dried in an oven (Precision) for 8 h, and then dry ball milled for 48 h to form a homogeneous powder. Approximately 20 g of the fuel-electrode powder is thoroughly mixed with 2 g of binder (10% polyvinyl alcohol, 20,000 MW, dissolved in water) and then dry pressed in a 57 mm diameter stainless-steel die in an automatic hydraulic press (Carver). Pressing pressure reaches 190 MPa (28,000 psi) for 10 s to form the green anode-support pellet.

### 2.2. Electrolyte and interlayer fabrication process

Thin layers of the electrolyte and interlayer are subsequently deposited onto the fuel electrode via ultrasonic spray coating. The electrolyte suspension solution is prepared by mixing stoichiometric ratios of  $\text{BaCO}_3$ ,  $\text{CeO}_2$ ,  $\text{ZrO}_2$ ,  $\text{Y}_2\text{O}_3$  and  $\text{Yb}_2\text{O}_3$  with a homogeneous mixture of binder, plasticizer and dispersant (Heraeus V-006, Alfa Aesar PEG 400 B21992, and Alfa Aesar PVP 40000 J62417, respectively). Mass fractions amount to 13 wt-% electrolyte precursor powder, 1 wt-% PEG 400, 1 wt-% PVP 40000, 2.5 wt-% V-006 A, 2.5 wt-%  $\alpha$ -terpineol (Alfa Aesar 16285), and 80 wt-% isopropanol. The solution is placed in a sonicator for 45 min, then vigorously mixed using a high-speed vortexer for five (5) minutes. This sequence is thrice repeated to achieve a homogeneous slurry.

Following mixing, the electrolyte slurry is deposited on the Ni-BCZYYb electrode support using an ultrasonic spray atomizer (Sonotek ALIGN). Dowd et al. [19] used a similar tool for catalyst infiltration into SOFC cathodes; Feng et al. [20] recently reported protonic-ceramic fuel-cell fabrication using ultrasonic spray. Processing parameters include nozzle power (3–4 W) and frequency (20 kHz), and liquid dispenser rate ( $0.3 \text{ mL min}^{-1}$ ) via syringe pump. Nitrogen carrier gas flows at  $6 \text{ L min}^{-1}$ . A 10%-Gd-doped ceria interlayer is also spray deposited atop the BCZYYb electrolyte. GDC slurry preparation is identical to that of the electrolyte, with the substitution of commercial tape-cast grade  $\text{Gd}_{0.1}\text{Ce}_{0.9}\text{O}_{1.95}$  powder (Fuelcellmaterials, GDC10-112101).

Following atomistic spray of the electrolyte and interlayer, green cells are placed on ceramic setter plates and sintered at 1450–1550 °C for 5 h. We note that the precursors in the fuel electrode and the electrolyte react to form single-phase BCZYYb while the electrochemical cell is simultaneously sintered and formed. This solid-state reactive sintering (SSRS), the combination of calcination and cell fabrication into a single firing step, can bring meaningful manufacturing-cost and time savings [21].

Magnesia-stabilized zirconia setters (Applied Ceramics SP-004369-043M) minimize materials interactions between the electrochemical cells and the kiln furniture; reactive sintering can enhance such problems. We find that “well seasoned” setters which have been repeatably used in the firing process minimize reactivity issues. Following sintering, the electrolyte and interlayer thicknesses are  $\sim 10$  and  $2 \mu\text{m}$ , respectively, while bulk shrinkage reaches  $\sim 25\%$ . As will be shown, the interlayer is discontinuous, with a more-variable thickness than found for the thicker electrolyte. The fuel electrode is subsequently polished using an automated grinder (LECO Spectrum System 1000) to remove any surface contamination and reduce cell thickness is  $\sim 0.8 \text{ mm}$ .

### 2.3. Air–steam electrode and current collectors

The  $\text{BaCo}_{0.4}\text{Fe}_{0.4}\text{Zr}_{0.1}\text{Y}_{0.1}\text{O}_{3-\delta}$  (BCPZY) air–steam electrode material is synthesized by a sol–gel method as described in Duan et al. [22]. This powder is mixed with 20 wt-% single-phase, SSRS-formed electrolyte powder to promote adherence with the electrolyte, and to potentially extend the length of the electrochemically active region. The composite electrode is mixed with a binder and dispersant (5 wt-% Heraeus V006-A and 20 wt-% Solperse 28000 diluted in alpha-terpineol, respectively) to form an ink that is brush-painted onto the electrolyte. The complete MEA is then sintered at 900 °C in air for five (5) h using a heating ramp rate of  $1\text{--}1.5 \text{ }^\circ\text{C min}^{-1}$ . The resulting cells have an active area of  $5 \text{ cm}^2$ . This is an order-of-magnitude increase in active area from prior button cells (less than  $0.5 \text{ cm}^2$ ), reflecting an encouraging measure of scalability of the protonic-ceramic materials set.

MEAs are packaged into unit- and multi-cell stacks as described in Le et al [7]. The MEAs are bonded to magnesia–alumina frames (Aremco 502-800) using an alumina-filled ceramic adhesive (Aremco Ceramabond 552). A thin gold paste (Heraeus, Au 200-03) is brush-painted onto the air–steam electrode, with silver wires (Alfa Aesar 41456) then attached using silver conductive paste to create a channel-like configuration.

#### 2.4. Stack electrochemical performance characterization

A laboratory-built test stand is used to characterize stack electrochemical performance. The stand includes a furnace (Applied Test Systems, Inc.) to control stack operating temperature, mass flow controllers (Alicat, M-series) to regulate the supply of H<sub>2</sub>, CH<sub>4</sub>, and Ar to the fuel electrode, and synthetic air (21% O<sub>2</sub>/79% Ar) to the air-steam electrode. Fuel and oxidizer flow rates to the stack are held at 200 sccm. Water vapor is added to either the fuel or oxidizer streams by flowing reactants through heated water bubblers. Bubbler temperature is tuned to achieve target humidification according to the Clausius–Clapeyron relation, and validated using a humidity sensor (Rotronic, Hygroflex).

An electronic load (Keithley 2400) measures DC power generation, while an impedance analyzer (Gamry Instruments, Reference 5000) probes the AC response. A data acquisition (U6-Pro, Labjack) and control system (National Instruments, LabView) is used to operate the stand.

Following assembly, gas hermeticity is confirmed through two independent measurements. Exhaust-gas composition is continuously measured using gas chromatography (Agilent, Micro GC 3000). Additionally, the volumetric flow rate of stack exhaust gases is continuously measured (DryCal Defender 530 Plus, Mesa Labs) and compared with reactants supplied. Overall, robust sealing is observed, reaching less than 10% leakage rate.

#### 2.5. Microstructure and diffraction analysis

The pre- and post-mortem microstructures of the stack components are characterized using a Field-Emission Scanning Electron Microscope (FE-SEM, JEOL JSM7000F) coupled with an Energy Dispersive X-ray Spectroscopy (EDAX) detector for elemental composition analysis. All crystallography data is obtained using a Philips X'Pert Pro MPD diffractometer (PANalytical, Almelo, Netherlands) with Cu-K<sub>α</sub> radiation, a tube voltage of 45 kV, and a tube current of 40 mA. X-ray diffraction (XRD) is performed at room temperature.

### 3. Results and discussion

#### 3.1. Fuel cell stability

The improvement in protonic-ceramic fuel-cell stability brought by the GDC interlayer is evident in Fig. 2. The interlayer reduces voltage degradation in our unit-cell stacks from 36% khr<sup>-1</sup> to 3.3% khr<sup>-1</sup> at 550 °C. Degradation rates are further lowered to 1% khr<sup>-1</sup> through slightly higher-temperature operation (600 °C) under CH<sub>4</sub>-H<sub>2</sub>O fuel, while thermally promoting internal reforming chemistry within the fuel electrode.

The lower operating temperatures are expected to improve stability in protonic ceramics by mitigating thermally driven degradation processes. However, we have observed highest fuel-cell stability when operating above 600 °C (Fig. 2b). The GDC interlayer brings improvements in stability, but at temperatures below 500 °C voltage degradation rates remain high.

Electron micrographs in Fig. 3 reveal the changes to the surface morphology brought by the interlayer. Rather than forming a continuous layer, the GDC particles form well-dispersed, unpercolated islands of 15–20 μm in diameter across the electrolyte. The cross-sectional of this layer has been reported in our previous works [7]. EDAX scans confirm gadolinium and cerium enrichment in the electrolyte surface.

SOFC developers have long used interlayers to mitigate unwanted materials interactions [23]. The 10%-mol gadolinium-doped ceria used in this study has high oxygen-ion conductivity and reasonable chemical stability at low temperatures. Li et al. [24] found GDC to reduce cathodic activation loss in PCFCs, attributing improvements to the GDC's mixed conductivity at temperatures below 400 °C [25]. While the performance and stability improvements brought by the GDC

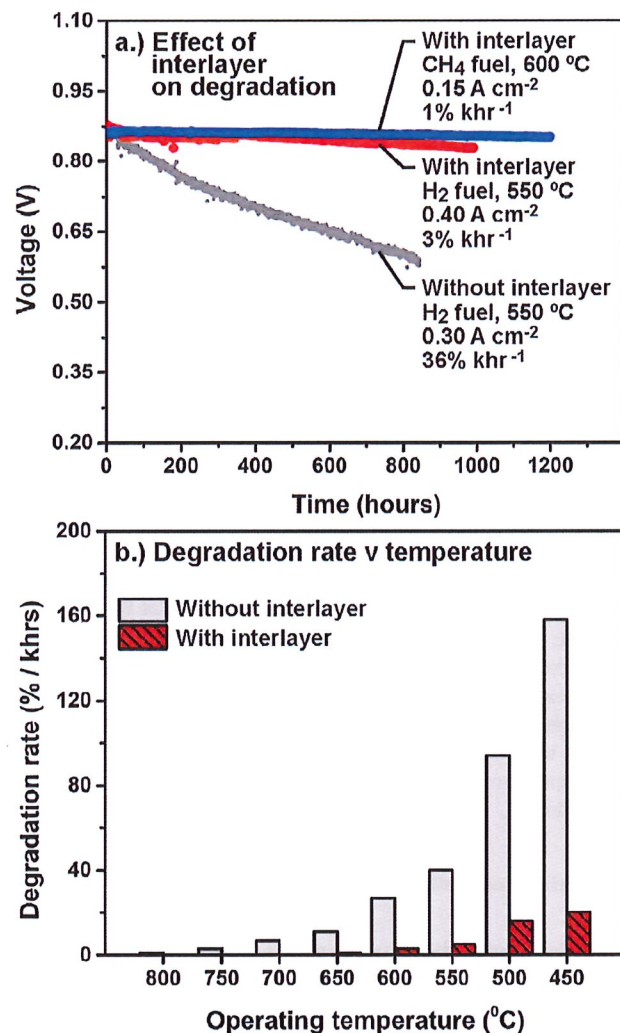


Fig. 2. (a) Protonic-ceramic fuel-cell stability under H<sub>2</sub> and CH<sub>4</sub> fuels; GDC interlayer and 600 °C operation reduce degradation to 1% khr<sup>-1</sup>; (b) impact of operating temperature on degradation rate, with the interlayer again promoting stability.

are encouraging, alternate interlayer materials can also be explored, presenting a rich area for future protonic-ceramics research.

Fig. 4 shows microstructural analysis of high-degradation, interlayer-free PCFCs following hundreds of hours of operation. Despite the high degradation rate of 36% khr<sup>-1</sup>, the microstructure in Fig. 4a shows none of the characteristic degradation processes found in higher-temperature SOFCs:

- the air-steam electrode remains highly porous with nano-scale structures and high surface area;
- the electrolyte remains dense, with no sign of grain separation;
- the nickel phase of the cermet fuel electrode displays high surface area, with no sign of coarsening;
- the electrode/electrolyte interfaces do not show evidence of delamination, pore generation, reaction or secondary phase formation.

The electrode–electrolyte interfaces appear well adhered, with excellent electrolyte percolation into the fuel electrode, facilitated by co-sintering of the fuel electrode with the electrolyte. The elemental line scans in Fig. 4b reveal no sign of nickel migration at the electrochemically-active zone. This is in sharp contrast to the nickel

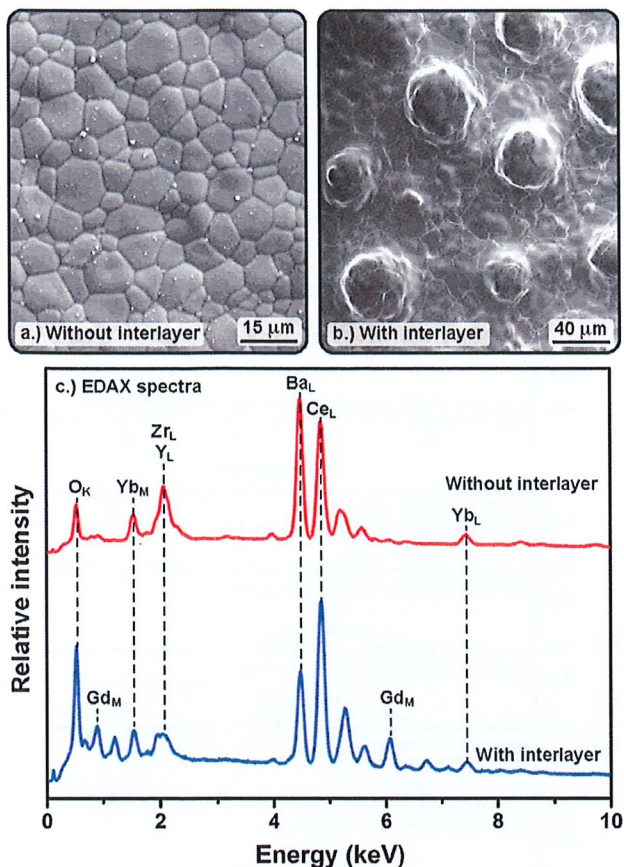


**Fig. 3.** Scanning electron micrographs of the electrolyte surface, (a) without interlayer; (b) with interlayer; (c) EDAX spectra of electrolyte surface with and without interlayer.

migration commonly observed in high-temperature SOFCs, where visible depletion of nickel is generally evident at the triple-phase boundary after long-term operation [11,26]. Changes in the intensity of Fe and Co found in the air–steam electrode are only observed at the electrode–electrolyte interface, indicating no interdiffusion of the Fe and Co ions between the BCZYYb electrolyte and the BCFZY air–steam electrode.

Nickel agglomeration, a common source of degradation in higher-temperature SOFCs [27–29], is also not observed. Rather, the nickel particles remain highly percolated within the anode body. Particle size remains less than 5 μm with homogeneously distributed micro-pores found across the nickel surface. The preservation of such high surface area over hundreds of hours of operation is encouraging for commercial viability.

We also find no evidence of chromium contamination in either electrode following longer-term PCFC-stack discharge at 550 °C. Fig. 4c compares the EDAX spectra of PCFC stacks following longer-term operation at 550 and 800 °C. Despite use of identical materials and testing protocols, we only detect chromium (5.4 keV) and silicon (1.7 keV) for the 800 °C sample after being tested for 200 h, with none found at 550 °C. The absence of chromium contamination from our longer-term PCFC stack tests provides encouraging evidence of how lower-temperature operation can effectively suppress chromium poisoning in PCFCs.

While these post-mortem characterizations present encouraging results regarding the stability of PCFC cell and stack materials, the cell shown in Fig. 4a and b nevertheless suffered from pronounced performance degradation which cannot be attributed to obvious chemical or microstructural cell changes. Even so, these degradation problems are

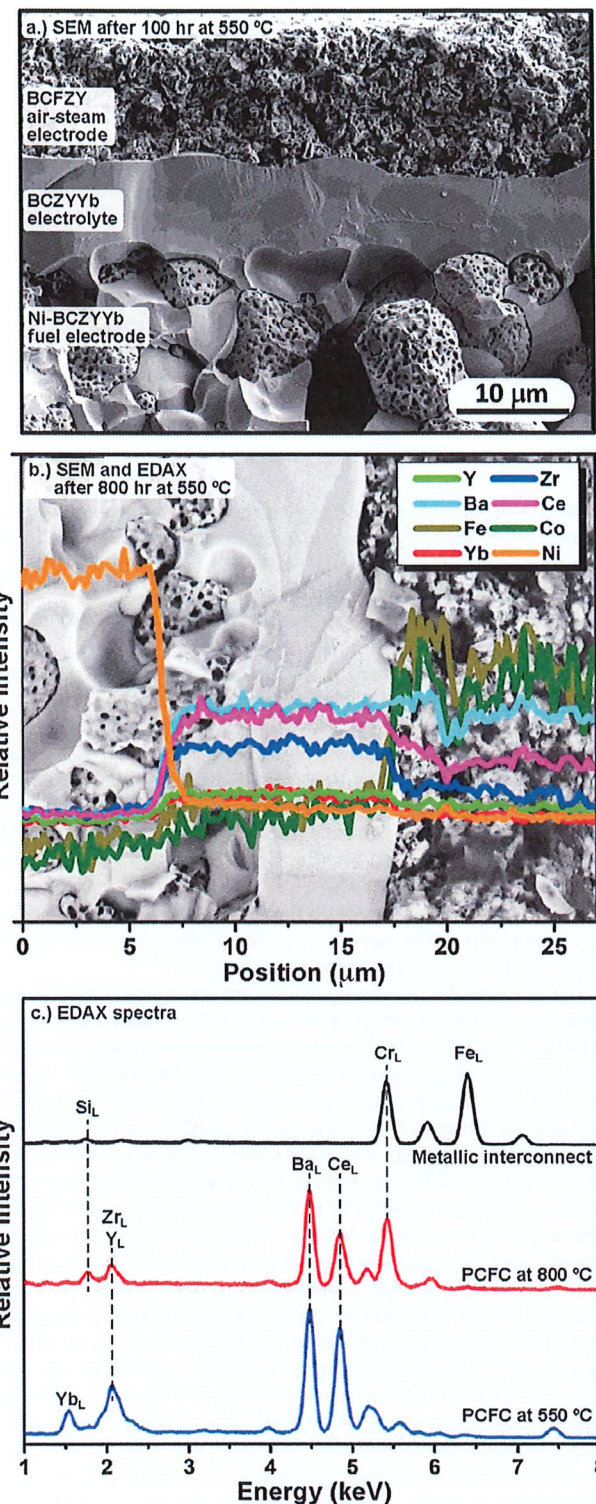


**Fig. 4.** (a) Electron micrograph of the PCFC fracture cross section following 800 hr of continuous operation at 550 °C; (b) EDAX elemental linescans overlaid onto cross-section micrograph; (c) EDAX spectra of BCFZY air–steam electrodes and metallic interconnect following long-term PCFC stack operation. Chromium is detected in the electrode operated at 800 °C, but absent from the lower temperature cell at 550 °C.

greatly mitigated through application of the GDC interlayer, suggesting that processes at the air–steam electrode/electrolyte interface may be central to protonic-ceramic cell degradation. The root causes of

degradation and its mitigation thus remain an active area of study. We have observed improved adherence of the air–steam electrode onto the electrolyte surface in the presence of the GDC interlayer. This could be tied to the respective basic and acidic nature of the H<sup>+</sup>- and O<sup>2-</sup>-ion-conducting materials. While electrode adherence has been a long-standing challenge in protonic-ceramic devices, we lack a definitive measure of electrode adherence to quantify this property and the improvement brought by the interlayer. We note the emergence of such characterization protocols through “benchmarking” workshops within the scientific community [30]. While electrode adherence is certainly critical, it is likely not the only source of degradation in these protonic ceramic cells. Our *in-situ* electrochemical impedance spectroscopy investigations during longer-term testing provide further insight into the dominant and fundamental degradation mechanisms in these protonic-ceramic cells, as presented in Section 3.3.

### 3.2. Electrolyzer stability

We have consistently found protonic ceramics to demonstrate better stability under electrolysis operation in comparison to fuel-cell mode. This is perhaps unexpected, as O<sup>2-</sup>-ion-conducting SOECs are reported to degrade three-times faster than their SOFC counterparts [31–33]. We have also found the interlayer to promote electrolyzer stability at steam feeds as high as 50%.

This behavior is captured in Fig. 5a, which shows the stability of protonic-ceramic unit-cell electrolysis stacks over 100 hr at 550 °C. The top chart reflects excellent PCEC stability at a high current density of 1.8 A cm<sup>-2</sup> and low steam-feed concentration of 10% H<sub>2</sub>O (balance air). After the initial voltage drop, which may be associated with the intermittent self-heating of the cell under high current or the reduction of nickel at the fuel-side TPB, the electrolyzer performance is found to be improved over the 100 hr of operation at 10% H<sub>2</sub>O. The driving voltage is reducing by 13% khr<sup>-1</sup>, despite the absence of the GDC interlayer in this electrolysis cell. In the second chart of Fig. 5a, boosting the steam feed to 20% increases the degradation rate to 49% khr<sup>-1</sup>, despite the lower current density of 0.5 A cm<sup>-2</sup>.

The dramatically improved stability brought by the GDC interlayer is shown in the bottom chart of 5a, where voltage degradation reduces to 1% khr<sup>-1</sup> at 0.5 A cm<sup>-2</sup> driving current despite a 50% steam feed. To the authors' knowledge, this is among the lowest PCEC degradation rates reported to date. Increasing the feed steam concentration is crucial for commercial viability, as it greatly impacts system-level efficiency; achieving high durability under high steam-feed concentration is critical. Additionally, high steam concentrations improve proton conduction through the BCZYYb electrolyte. Proton concentration is dependent upon steam concentration to the 1/4 power [34,35], while the electron-hole concentration is commensurately reduced. Thus, higher P<sub>H<sub>2</sub>O</sub> concentration strongly boosts PCEC Faradaic efficiency.

In Fig. 5b, the EIS scans reveal the impact of steam concentration on the cell resistances as measured by AC impedance at open-circuit voltage (OCV). Both ohmic and polarization resistances are stable under 10% steam, but dramatically increase over time when the steam concentration is above 20%. The polarization resistance increases drastically at a much shorter exposure time when the humidity increases to 30 or 40%. This sharp increase in resistance is consistent with electrode delamination from the electrolyte. Post-mortem XRD analysis reveals no new phase formation in the BCFZY electrode material under high steam.

These cells also demonstrate stable impedance at steam-feed concentrations up to 50%, consistent with the low degradation rates observed during long-term PCEC operation in cells incorporating the GDC interlayer. It is noteworthy that the DC resistance is slightly higher for the interlayer-containing PCEC as compared to PCECs without the interlayer, (e.g., ~0.7 vs 0.5 Ω cm<sup>2</sup> at 550 °C and 50% H<sub>2</sub>O). The electrode polarization resistances of the interlayer-based cell remain stable throughout the 100 hr of electrolysis operation at these higher-steam

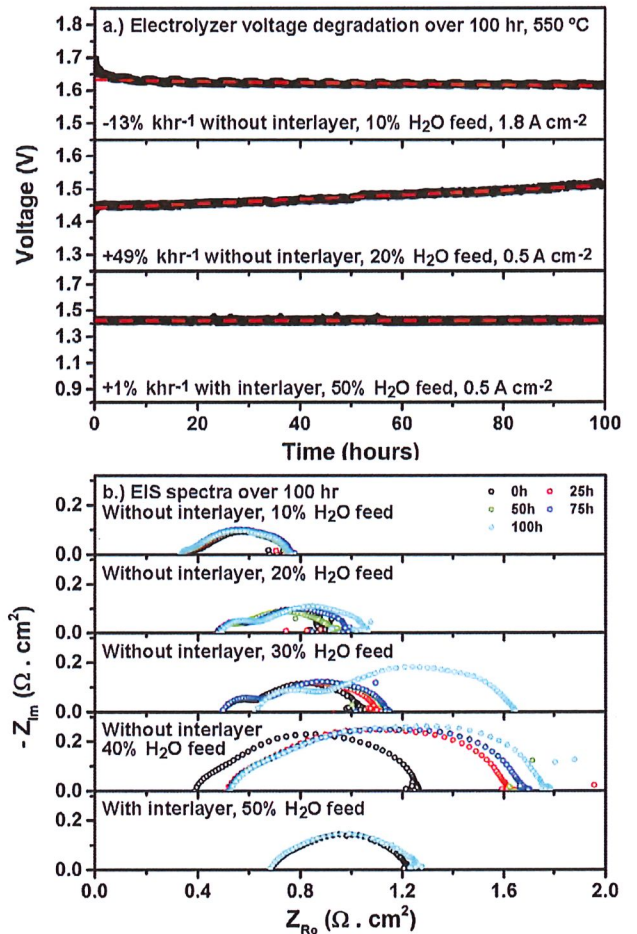


Fig. 5. (a) PCEC stability at several operating conditions; (b) electrolyzer impedance spectra measured at open-circuit condition during the stability experiments.

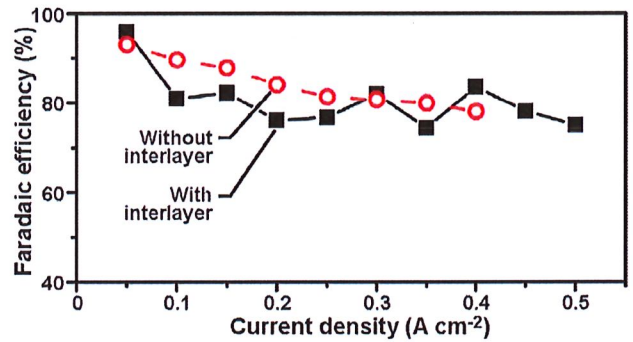


Fig. 6. Faradaic efficiency of unit-cell protonic-ceramic electrolyzer stack as a function of current density, with and without interlayer. The interlayer is not found to have a pronounced effect on Faradaic efficiency. Operating conditions: 10% H<sub>2</sub>O + 90% air and 100% H<sub>2</sub> fed to air–steam and fuel electrodes, respectively; 550 °C.

conditions. In contrast, the polarization resistances in the absence of the interlayer increase dramatically during operation, even under lower steam-feed conditions.

The mixed ionic–electronic conduction behavior of protonic-ceramic electrolyte materials presents a principal concern for the technology and remains an active area of research. Transport of oxygen vacancies and small polarons in parallel with protons is particularly problematic under electrolysis operation [36]. Higher PCEC efficiencies can be

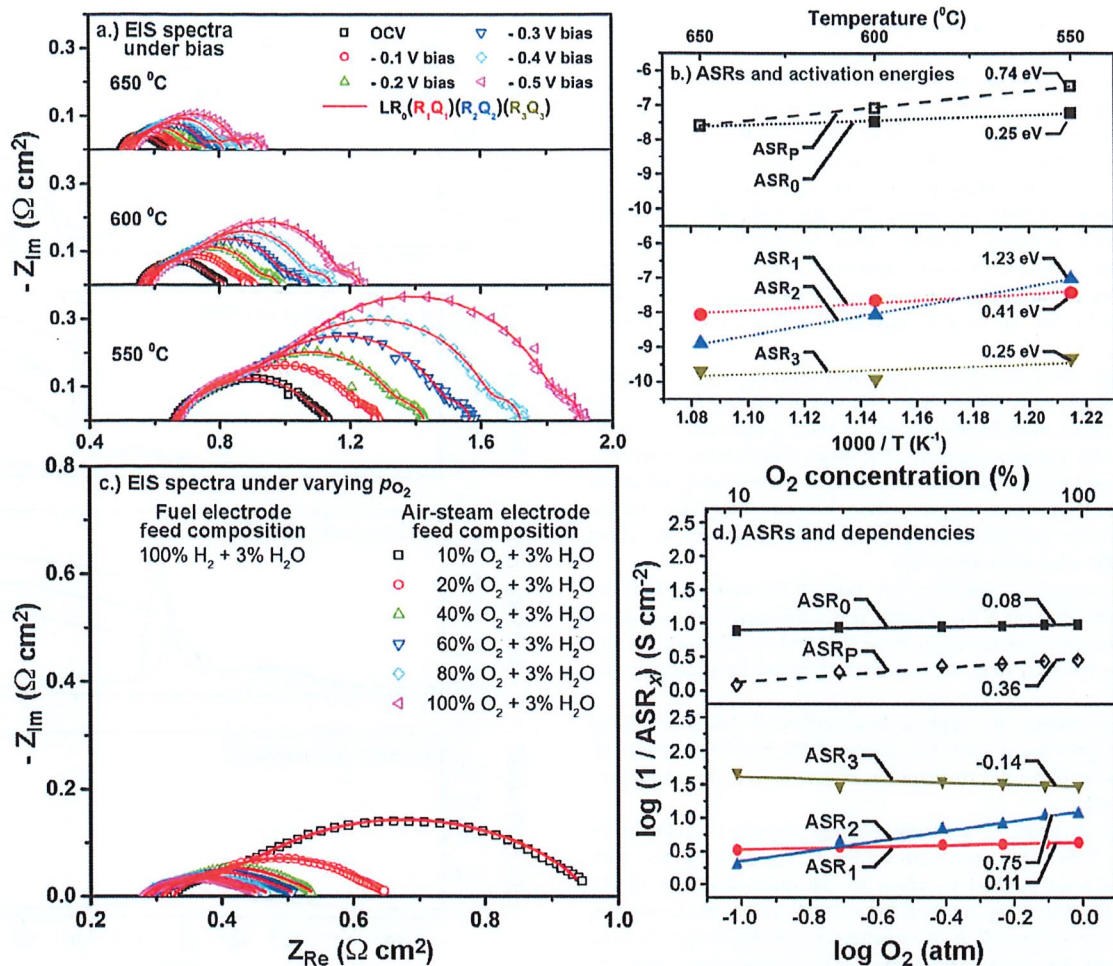


Fig. 7. (a) Electrochemical impedance spectra of protonic-ceramic cell under externally applied bias, with equivalent-circuit model fit; (b) area-specific resistances and activation energies of circuit components under 0.5 V bias; (c) EIS at varying oxygen partial pressure in the air-steam electrode feed gas; and (d) area-specific resistances and dependencies on oxygen partial pressure.

realized through higher steam-feed concentrations and lower operating temperatures. However, both can be detrimental to PCEC lifetime.

The regulation of mixed conduction to optimize device performance presents an active field of study. In this work, we limit our questions to the impact of the interlayer on Faradaic efficiency, and find its impact to be modest. As shown in Fig. 6, Faradaic efficiency decreases from its 95% maximum at 0.05 A cm<sup>-2</sup> to ~80% at 0.5 A cm<sup>-2</sup>. The interlayer brings slightly lower Faradaic efficiency at the lower current densities ( $\leq 0.25$  A cm<sup>-2</sup>). These data reflect unit-cell stack performance at 550 °C and 10% H<sub>2</sub>O feed, leading to fairly high electronic leakage and hence relatively low Faradaic efficiency.

The use of an interlayer to mitigate the unwanted materials interactions has been widely reported in the SOFC and SOEC literature [23]. The selection of interlayer material remains an open research question; we have selected 10%-mol gadolinium-doped ceria due to its high oxygen-ion conductivity and reasonable chemical stability at low temperatures. Li et al. [24] found additional GDC benefits to PCFC's through reduction in the cathodic-activation losses. This performance gain is attributed to the mixed conductivities of the nano-granular GDC at temperatures below 400 °C [25,37]. While our operating temperature is higher than these previous reports, the high density of GDC grain boundaries and lattice defects may still promote the oxygen reduction reactions to bring electrochemical performance benefits.

### 3.3. EIS and DRT analyses

Electrochemical impedance spectroscopy can provide clues to degradation root causes. Utilizing “fresh” cells, we executed a range of EIS studies from 550–650 °C under 0–0.5 V bias (fuel-cell mode). Gas conditions are fixed at 100% H<sub>2</sub> and air + 10% steam at the fuel and air-steam electrodes, respectively. We find that a four-component equivalent-circuit model  $LR_0(RQ)_1(RQ)_2(RQ)_3$  accurately captures the typical impedance responses from our cells, as shown in Fig. 7a. Consistent with previous studies [38–40], we attribute the characteristic phenomena associated with these equivalent circuit processes as:

1.  $L$  represents the inductance resistance;
2.  $R_0$  represents the ohmic loss commonly associated with charge transport through the electrolyte;
3.  $R_1Q_1$  represents charge transfer associated with a characteristic pseudo-capacitance of  $\sim 10^{-4}$ – $10^{-3}$  (F cm<sup>2</sup>);
4.  $R_2Q_2$  represents surface diffusion associated with a typical pseudo-capacitance of  $10^{-3}$ – $10^{-2}$  (F cm<sup>2</sup>);
5.  $R_3Q_3$  represents dissociative adsorption/dissociation of the gaseous species or concentration losses within the electrode. The pseudo-capacitance of both phenomena is typically observed at  $10^{-1}$ – $10^1$  (F cm<sup>2</sup>).

The activation energies of each of these elementary processes can be determined through Arrhenius analysis of their corresponding

temperature-dependent area-specific resistances ( $ASR_i$ ), as summarized in Fig. 7b for fuel-cell operation at 0.5 V bias.

The activation energies of  $ASR_0$  and  $ASR_p$  are 0.25 and 0.74 eV, consistent with the previously reported values for protonic-ceramic electrochemical cells [25,35,41]. Analysis of the elemental polarization resistances embedded within  $ASR_p$  reveals that each behave differently with respect to the operating temperature.  $ASR_1$  shows a moderate activation energy of 0.41 eV, while  $ASR_2$  has a significantly higher value of 1.23 eV, and  $ASR_3$  exhibits a small  $E_a$  of 0.25 eV.

Further EIS measurements were executed over a range of oxygen partial pressure fed to the air–steam electrode. Cell temperature is held at 550 °C, while the fuel feed is fixed as humidified H<sub>2</sub>. Results are shown in Fig. 7c.

Both ohmic and polarization resistances decrease with increasing oxygen partial pressure. We attribute this to the increase in electronic conductivity under oxidizing environments and the increasing chemical potential of the gaseous reactant. The total polarization resistance shows a stronger oxygen dependence (0.36) than the ohmic resistance (0.08). This indicates that oxygen activity has a greater effect on the electrode reaction process in comparison to its effect on the mixed transport in the electrolyte (Fig. 7d).

The strong oxygen dependence on  $ASR_2$  (0.75) confirms that the oxygen surface diffusion is the limiting process during fuel-cell operation. As the oxygen concentration increases, higher hole conductivity and exchange reaction rates at the electrochemical interfaces can be realized [42].

For further insight, we apply a Distribution of Relaxation Time (DRT) fitting package to our EIS results. DRT has been found effective to deconvolute the overlapping effects present in impedance spectra [43–45].

We utilize a robust DRT fitting package recently developed by Huang et al. [46]. This open-source DRT fitting tool utilizes a hierarchical Bayesian method to adapt to the error structure of the impedance data, removing the need for manual tuning. We found that this model works quite well to fit and analyze impedance spectra from our degradation experiments, achieving residual errors of less than 1%.

Fig. 8 compares DRT responses of cells with and without the GDC interlayer over 100 hr of fuel-cell operation at 550 °C. The AC perturbation magnitude is fixed at 10 mV, while potentiostatic EIS is measured at both OCV and 0.5 V bias in fuel-cell mode. The current density is elevated to 0.3 A cm<sup>-2</sup>, corresponding to a 0.5 V overpotential, accelerating any potential degradation. This load is applied throughout the 100 h test and only interrupted by the impedance measurements.

In the absence of the interlayer (Fig. 8a and b), it is clear that there are two major time-dependent peaks present under both OCV and bias conditions. At OCV, the low-frequency peak grows rapidly in time, accounting for the high performance degradation (> 100% kWh<sup>-1</sup>) observed in this cell, while the medium-frequency peak actually attenuates slightly over the same time period. In contrast, at 0.5 V bias, the medium-frequency peak (10<sup>2</sup>–10<sup>1</sup>) increases while the low-frequency peak (10<sup>1</sup>–10<sup>0</sup>) attenuates over time. The low-frequency peak also shifts about one order of magnitude lower in frequency compared to OCV. The peak-shifting phenomenon indicates that the gas dissociation/adsorption process has higher capacitance under load than at OCV, likely reflecting increased coverage of charged adsorbate species. We hypothesize that under high fuel-cell bias, the competition between oxygen reduction and water evolution at the air side, coupled with hole removal, may trigger a degeneration process at the air–steam electrode.

In the presence of GDC interlayer (Fig. 8c and d), the DRT response is stable under OCV conditions for the 100 hr test, while under bias the medium-frequency peak actually decreases in time, in direct contrast to the response of the interlayer-free cell. These results are consistent with the greatly enhanced stability observed for interlayer-based cells. Additionally, the interlayer cell demonstrates no frequency shifts of DRT

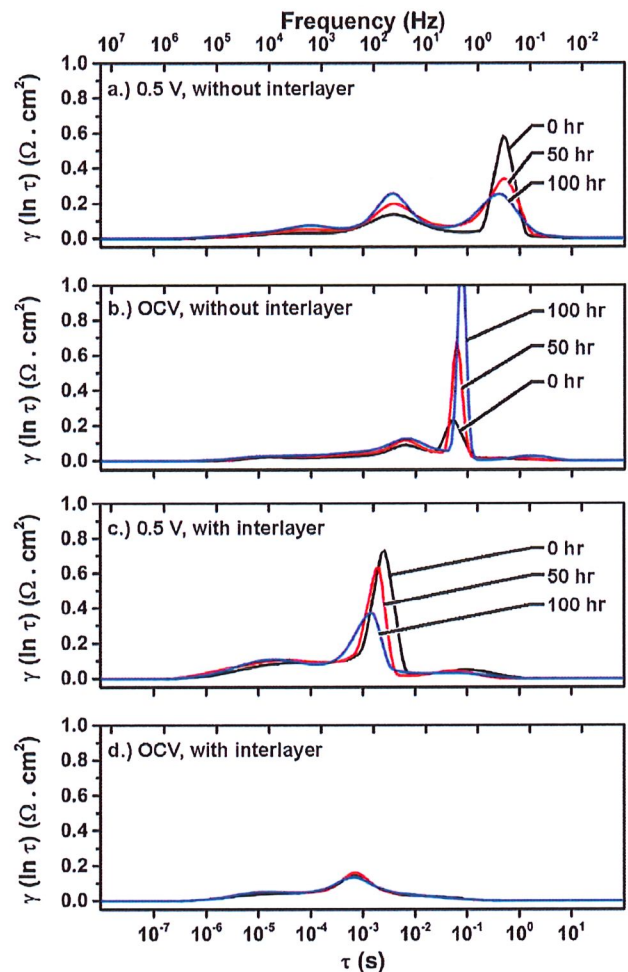


Fig. 8. Distribution of relaxation times over 100 hr of continuous protonic-ceramic cell operation: (a) without interlayer at 0.5 V potential; (b) without interlayer at open-circuit voltage; (c) with interlayer at 0.5 V potential; (d) with interlayer at open-circuit voltage.

peaks under bias. This suggests that the GDC interlayer may play a role in mitigating the deleterious accumulation of excess charged adsorbate species on the active electrode surface during electrode polarization. Finally, due to the decrease in the magnitude of the medium-frequency peak under bias, we speculate that the interlayer may play a role in improving oxygen surface diffusion. The additional oxygen vacancies generated by the interlayer may provide an alternative pathway for oxygen-reduction reactions.

#### 4. Conclusion

This work summarizes our observations of degradation behavior in protonic-ceramic fuel cells and electrolyzers. We find no evidence of microstructural coarsening or chromium evaporation in protonic-ceramic stacks following hundreds of hours of testing. Despite the lack of obvious chemical or microstructural changes, we nevertheless observe significant fuel-cell performance degradation at temperatures below 550 °C. In contrast, the stack stability in electrolysis mode is excellent, indicating the degradation mechanism is strongly tied to electrochemical processes that occur during fuel-cell operation.

We can successfully mitigate protonic-ceramic degradation by modifying the air–steam electrode–electrolyte interface with a 10%-doped gadolinium ceria interlayer. The interlayer is deposited atop the electrolyte surface, followed by high-temperature reactive sintering. SEM

analysis reveals a dense electrolyte layer decorated by discontinuous GDC particles  $\sim$ 10–20  $\mu\text{m}$  in diameter.

A unit-cell stack equipped with this MEA configuration, using methane and air as fuels, demonstrates a degradation rate of 1.2%  $\text{khr}^{-1}$  over 1200 h of continuous fuel-cell operation at 550 °C. The interlayer also promotes stability in electrolysis mode under high steam feed. In the absence of the interlayer, electrolysis performance degrades at  $\text{H}_2\text{O}$  mole fractions exceeding 20%. With the interlayer, we successfully demonstrate stable electrolysis operation at 50% humidity with a degradation rate of 1%  $\text{khr}^{-1}$  at 0.5 A/cm<sup>2</sup>, 550 °C.

Our analysis of AC impedance spectra provides insight to the degradation behaviors observed in our cells. Despite the complex competition between the multiple elementary electrochemical processes proceeding in concert during cell operation, some fundamental understanding of the degradation mechanisms in PCFCs can be interpreted from the EIS results.

The oxygen surface diffusion occurring at  $\sim$ 10–100 Hz is found to be the PCFC performance-limiting factor under the temperature and reactant concentration conditions studied here. The impact of this electrochemical process toward the overall cell resistance become increasingly important at lower temperatures, lower oxygen pressures, and higher fuel-cell-mode bias. We attribute this behavior to the slow kinetics of the air–steam electrode.

Using Distribution of Relaxation Time analysis, the cell degradation is tied to oxygen surface diffusion and gas dissociation/adsorption appearing at  $\sim$ 10–100 and 10–0.1 Hz. The interlayer is found to effectively mitigate the growth of the corresponding resistances, greatly reducing the overall cell-degradation rate. The root cause of this degradation mechanism remains an active area of study, as does the broad field of degradation in proton-conducting electroceramics.

#### CRediT authorship contribution statement

**Long Q. Le:** Lead researcher, Formal analysis, Writing and editing manuscript, Investigation. **Charlie Meisel:** Formal analysis, Methodology, Writing – review and editing original draft. **Carolina H. Hernandez:** Microstructural analysis, Methodology, Validation. **Jake Huang:** Implement EIS/DRT data analysis, Data curation, Validation. **Youdong Kim:** Methodology, Validation. **Ryan O’Hayre:** Conceptualization, Visualization, Writing – review and editing, Funding acquisition. **Neal P. Sullivan:** Supervision, Conceptualization, Writing – review & editing final draft, Funding acquisition.

#### Declaration of competing interest

As required through contractual obligation our manuscript includes the following disclosure: The information data or work presented herein was funded in part by the Advanced Research Projects Agency-Energy (ARPA-E), U.S. Department of Energy under Award Number DE-AR0000493. The views and opinions of authors expressed herein do not necessarily state or reflect those of the United States government or any agency thereof.

#### Acknowledgments

The information, data, or work presented herein was funded in part by the Advanced Research Projects Agency - Energy, U.S. Department of Energy, under Award Number DE-AR0000493. The views and opinions of authors expressed herein do not necessarily state or reflect those of the United States Government or any agency thereof. The authors thank Mr. Charles Reid and Mr. Chris Chmura for illustrations shown in Fig. 1.

#### References

- [1] C. Duan, R. Kee, H. Zhu, N. Sullivan, L. Zhu, L. Bian, D. Jennings, R. O’Hayre, Highly efficient reversible protonic ceramic electrochemical cells for power generation and fuel production, *Nature Energy* 4 (3) (2019) 230–240, <http://dx.doi.org/10.1038/s41560-019-0333-2>.
- [2] Z. Tao, M. Fu, Y. Liu, Y. Gao, H. Tong, W. Hu, L. Lei, L. Bi, High-performing proton-conducting solid oxide fuel cells with triple-conducting cathode of  $\text{Pr}_{0.5}\text{Ba}_{0.5}(\text{Co}_{0.7}\text{Fe}_{0.3})\text{O}_{3-\delta}$  tailored with W, *Int. J. Hydrogen Energy* 47 (2022) 1947–1953, <http://dx.doi.org/10.1016/j.ijhydene.2021.10.145>.
- [3] S.H. Morejudo, R. Zanón, S. Escalástico, I. Yuste-Tirados, H. Malerød-Fjeld, P.K. Vestre, W.G. Coors, A. Martínez, T. Norby, J.M. Serra, C. Kjølseth, Direct conversion of methane to aromatics in a catalytic co-ionic membrane reactor, *Science* 353 (6299) (2016) 563–566, <http://dx.doi.org/10.1126/science.aag0274>, URL <https://science.sciencemag.org/content/353/6299/563>.
- [4] I. Kalaitzidou, A. Katsounis, T. Norby, C.G. Vayenyas, Electrochemical promotion of the hydrogenation of  $\text{CO}_2$  on Ru deposited on a BZY proton conductor, *J. Catalysis* 331 (2015) 98–109.
- [5] V. Kyriakou, I. Garagounis, A. Vourros, E. Vasileiou, M. Stoukides, An electrochemical Haber-Bosch process, *Joule* 4 (1) (2020) 142–158, <http://dx.doi.org/10.1016/j.joule.2019.10.006>, URL <http://www.sciencedirect.com/science/article/pii/S2542435119305227>.
- [6] L. Zhu, C. Cadigan, C. Duan, J. Huang, L. Bian, C. Le, V. Avance, R. O’Hayre, N.P. Sullivan, Improving performance and enabling reversible operation in ammonia-fed protonic ceramic fuel cells via a novel Ru-B2CA catalyst, *Commun. Chem.* 4 (121) (2021) 230–240, <http://dx.doi.org/10.1038/s42004-021-00559-2>.
- [7] L.Q. Le, C.H. Hernandez, M.H. Rodriguez, L. Zhu, C. Duan, H. Ding, R.P. O’Hayre, N.P. Sullivan, Proton-conducting ceramic fuel cells: Scale up and stack integration, *J. Power Sources* 482 (2021) 228868, <http://dx.doi.org/10.1016/j.jpowsour.2020.228868>, URL <https://linkinghub.elsevier.com/retrieve/pii/S0378775320311721>.
- [8] R. Pinsky, P. Sabharwall, J. Hartvigsen, J. O’Brien, Comparative review of hydrogen production technologies for nuclear hybrid energy systems, *Prog. Nucl. Energy* 123 (2020) 103317, <http://dx.doi.org/10.1016/j.pnucene.2020.103317>, URL <https://www.sciencedirect.com/science/article/pii/S014919702030069X>.
- [9] K. Ferguson, A. Dubois, K. Albrecht, R.J. Braun, High performance protonic ceramic fuel cell systems for distributed power generation, *Energy Convers. Manage.* 248 (2021) 114763, <http://dx.doi.org/10.1016/j.enconman.2021.114763>, URL <https://www.sciencedirect.com/science/article/pii/S0196890421009390>.
- [10] M.Z. Khan, M.T. Mehran, R.H. Song, J.W. Lee, S.B. Lee, T.H. Lim, A simplified approach to predict performance degradation of a solid oxide fuel cell anode, *J. Power Sources* 391 (2018) 94–105, <http://dx.doi.org/10.1016/j.jpowsour.2018.04.080>.
- [11] M.B. Mogensen, A. Hauch, X. Sun, M. Chen, Y. Tao, S.D. Ebbesen, K.V. Hansen, P.V. Hendriksen, Relation between Ni particle shape change and Ni migration in Ni-YSZ electrodes – A hypothesis, *Fuel Cells* 17 (2017) 434–441, <http://dx.doi.org/10.1002/fuce.201600222>.
- [12] A. Gunji, C. Wen, J. Otomo, T. Kobayashi, K. Ukai, Y. Mizutani, H. Takahashi, Carbon deposition behaviour on Ni-ScSZ anodes for internal reforming solid oxide fuel cells, *J. Power Sources* 131 (2004) 285–288, <http://dx.doi.org/10.1016/j.jpowsour.2003.11.086>.
- [13] Z. Tao, M. Fu, Y. Liu, A mini-review of carbon-resistant anode materials for solid oxide fuel cells, *Sustain. Energy Fuels* 5 (2021) 5420–5430, <http://dx.doi.org/10.1039/D1SE01300A>.
- [14] J. Nielsen, A. Hagen, Y.L. Liu, Effect of cathode gas humidification on performance and durability of solid oxide fuel cells, *Solid State Ion.* 181 (11) (2010) 517–524, <http://dx.doi.org/10.1016/j.ssi.2010.02.018>, URL <http://www.sciencedirect.com/science/article/pii/S0167273810000937>.
- [15] B. Hu, M. Keane, M.K. Mahapatra, P. Singh, Stability of strontium-doped lanthanum manganite cathode in humidified air, *J. Power Sources* 248 (2014) 196–204, <http://dx.doi.org/10.1016/j.jpowsour.2013.08.098>, URL <http://www.sciencedirect.com/science/article/pii/S0378775313014481>.
- [16] R. Michael, A. Ashish, S. Prabhakar, Solid oxide electrochemical systems: Material degradation processes and novel mitigation approaches, *Materials* (2018).
- [17] S.P. Jiang, L. Christiansen, K. Foged, Effect of glass sealant materials on microstructure and performance of Sr-doped LaMnO<sub>x</sub> cathodes, *J. Mater. Sci. Lett.* (2001).
- [18] C. Duan, R.J. Kee, H. Zhu, C. Karakaya, Y. Chen, S. Ricote, A. Jarry, E.J. Crumlin, D. Hook, R. Braun, N.P. Sullivan, R. O’Hayre, Highly durable, coking and sulfur tolerant, fuel-flexible protonic ceramic fuel cells, *Nature* 557 (7704) (2018) 217–222, <http://dx.doi.org/10.1038/s41586-018-0082-6>.
- [19] R.P. Dowd, S. Lee, Y. Fan, K. Gerdes, Engineering the solid oxide fuel cell electrocatalyst infiltration technique for industrial use, *Int. J. Hydrogen Energy* 41 (2016) <http://dx.doi.org/10.1016/j.ijhydene.2016.06.015>.
- [20] W. Feng, W. Wu, C. Jin, M. Zhou, W. Bian, W. Tang, J.Y. Gomez, R. Boardman, D. Ding, Exploring the structural uniformity and integrity of protonic ceramic thin film electrolyte using wet powder spraying, *J. Power Sources Adv.* 11 (2021) 100067.

- [21] A. Dubois, S. Ricote, R.J. Braun, Benchmarking the expected stack manufacturing cost of next generation, intermediate-temperature protonic ceramic fuel cells with solid oxide fuel cell technology, *J. Power Sources* 369 (2017) 65–77, <http://dx.doi.org/10.1016/j.jpowsour.2017.09.024>, URL <http://www.sciencedirect.com/science/article/pii/S0378775317311837>.
- [22] C. Duan, J. Tong, M. Shang, S. Nikodemski, M. Sanders, S. Ricote, A. Almansoori, R. O'Hayre, Readily processed protonic ceramic fuel cells with high performance at low temperatures, *Science* 349 (6254) (2015) 1321–1326, <http://dx.doi.org/10.1126/science.aab3987>, URL <https://science.sciencemag.org/content/349/6254/1321>.
- [23] M. Shiono, K. Kobayashi, T. Lan Nguyen, K. Hosoda, T. Kato, K. Ota, M. Dokiya, Effect of  $\text{CeO}_2$  interlayer on  $\text{ZrO}_2$  electrolyte/ $\text{La}(\text{Sr})\text{CoO}_3$  cathode for low-temperature SOFCs, *Solid State Ion.* 170 (1) (2004) 1–7, <http://dx.doi.org/10.1016/j.ssi.2004.02.018>, URL <http://www.sciencedirect.com/science/article/pii/S0167273804001018>.
- [24] Y. Li, S. Wang, P.C. Su, Proton-conducting micro-solid oxide fuel cells with improved cathode reactions by a nanoscale thin film gadolinium-doped ceria interlayer, *Sci. Rep.* 6 (2016) <http://dx.doi.org/10.1038/srep22369>.
- [25] Y. Meng, J. Gao, Z. Zhao, J. Amoroso, J. Tong, K.S. Brinkman, Review: Recent progress in low-temperature proton-conducting ceramics, *J. Mater. Sci.* 54 (2019) <http://dx.doi.org/10.1007/s10853-019-03559-9>.
- [26] M. Trini, A. Hauch, S.D. Angelis, X. Tong, P.V. Hendriksen, M. Chen, Comparison of microstructural evolution of fuel electrodes in solid oxide fuel cells and electrolysis cells, *J. Power Sources* 450 (2020) <http://dx.doi.org/10.1016/j.jpowsour.2019.227599>.
- [27] D. The, S. Grieshammer, M. Schroeder, M. Martin, M.A. Daroukh, F. Tietz, J. Scheffold, A. Brisse, Microstructural comparison of solid oxide electrolyser cells operated for 6100 h and 9000 h, *J. Power Sources* 275 (2015) 901–911, <http://dx.doi.org/10.1016/j.jpowsour.2014.10.188>.
- [28] M. Hubert, J. Laurencin, P. Cloetens, B. Morel, D. Montinaro, F. Lefebvre-Joud, Impact of nickel agglomeration on solid oxide cell operated in fuel cell and electrolysis modes, *J. Power Sources* 397 (2018) 240–251, <http://dx.doi.org/10.1016/j.jpowsour.2018.06.097>.
- [29] N.H. Menzler, D. Sebold, Y.J. Sohn, S. Zischke, Post-test characterization of a solid oxide fuel cell after more than 10 years of stack testing, *J. Power Sources* 478 (2020) <http://dx.doi.org/10.1016/j.jpowsour.2020.228770>.
- [30] Y.-S. Chou, Test ID: HTE-P-14, Contact Layer Bonding Strength and Thermal Cycle Stability, Tech. rep., Pacific Northwest National Laboratory, Richmond, WA, USA, 2019.
- [31] M.S. Sohal, Degradation in Solid Oxide Cells During High Temperature Electrolysis, Idaho National Laboratory, Idaho Falls, Idaho 83415, 2009.
- [32] B. Ramamurthi, N. Minh, J. Guan, J. Ruud, J. Hong, P. Riley, D. Weng, High Performance Flexible Reversible Solid Oxide Fuel Cell, GE Global Research Center Final Report for DOE Cooperative Agreement, 2016.
- [33] A. Hauch, S.D. Ebbesen, S.H. Jensen, M. Mogensen, Solid oxide electrolysis cells: Microstructure and degradation of the Ni/yttria-stabilized zirconia electrode, *J. Electrochim. Soc.* 155 (2008) B1184, <http://dx.doi.org/10.1149/1.2967331>.
- [34] E. Vøllestad, R. Strandbakke, M. Tarach, D. Catalán-Martínez, M.-L. Fontaine, D. Beaff, D.R. Clark, J.M. Serra, T. Norby, Mixed proton and electron conducting double perovskite anodes for stable and efficient tubular proton ceramic electrolyzers, *Nature Mater.* 18 (7) (2019) 752–759, <http://dx.doi.org/10.1038/s41563-019-0388-2>.
- [35] H. Zhu, S. Ricote, C. Duan, R.P. O'Hayre, R.J. Kee, Defect chemistry and transport within dense  $\text{BaCe}_{0.7}\text{Zr}_{0.1}\text{Y}_{0.1}\text{Yb}_{0.1}\text{O}_{3-\delta}$  (BCZYYb) proton-conducting membranes, *J. Electrochim. Soc.* 165 (2018) F845–F853, <http://dx.doi.org/10.1149/2.1091810jes>.
- [36] H. Zhu, S. Ricote, R.J. Kee, Faradaic efficiency in protonic-ceramic electrolysis cells, *J. Phys. Energy* (2021) URL <https://iopscience.iop.org/article/10.1088/2515-7655/ac3729>.
- [37] L. Malavasi, C. Fisher, M.S. Islam, Oxide-ion and proton conducting electrolyte materials for clean energy applications: Structural and mechanistic features, *Chem. Soc. Rev.* 39 (2010) 4370–4387, <http://dx.doi.org/10.1039/b915141a>.
- [38] R. Wang, Z. Sun, Y. Lu, S. Gopalan, S.N. Basu, U.B. Pal, Comparison of chromium poisoning between lanthanum strontium manganese and lanthanum strontium ferrite composite cathodes in solid oxide fuel cells, *J. Power Sources* 476 (2020) <http://dx.doi.org/10.1016/j.jpowsour.2020.228743>.
- [39] M.Y. Lu, R. Scipioni, B.K. Park, T. Yang, Y.A. Chart, S.A. Barnett, Mechanisms of  $\text{PrO}_x$  performance enhancement of oxygen electrodes for low and intermediate temperature solid oxide fuel cells, *Mat. Today Energy* 14 (2019) <http://dx.doi.org/10.1016/j.mtener.2019.100362>.
- [40] S.H. Jensen, A. Hauch, P.V. Hendriksen, M. Mogensen, N. Bonanos, T. Jacobsen, A method to separate process contributions in impedance spectra by variation of test conditions, *J. Electrochim. Soc.* 154 (2007) B1325, <http://dx.doi.org/10.1149/1.2790791>.
- [41] S. Ricote, N. Bonanos, H.-J. Wang, R. Haugsrud, Conductivity, transport number measurements and hydration thermodynamics of  $\text{BaCe}_{0.5}\text{Zr}_{0.7}\text{Y}_{0.1-\delta}\text{Ni}_y\text{O}_{3-\delta}$ , *Solid State Ion.* 185 (1) (2011) 11–17.
- [42] H. Zhu, S. Ricote, W.G. Coors, R. Kee, Interpreting equilibrium-conductivity and conductivity-relaxation measurements to establish thermodynamic and transport properties for multiple charged defect conducting ceramics, *Faraday Discuss.* 182 (2015) 49–74.
- [43] T.H. Wan, M. Saccoccia, C. Chen, F. Ciucci, Influence of the discretization methods on the distribution of relaxation times deconvolution: Implementing radial basis functions with DRTtools, *Electrochim. Acta* 184 (2015) <http://dx.doi.org/10.1016/j.electacta.2015.09.097>.
- [44] B.A. Boukamp, Derivation of a distribution function of relaxation times for the (fractal) finite length warburg, *Electrochim. Acta* 252 (2017) <http://dx.doi.org/10.1016/j.electacta.2017.08.154>.
- [45] B.A. Boukamp, A. Rolle, R.N. Vannier, R.K. Sharma, E. Djurado, Electrostatic spray deposited  $\text{Ca}_3\text{Co}_4\text{O}_{9+\delta}$  and  $\text{Ca}_3\text{Co}_4\text{O}_{9+\delta}/\text{Ce}_{0.9}\text{Gd}_{0.1}\text{O}_{1.95}$  cathodes for SOFC: A comparative impedance analysis study, *Electrochim. Acta* 362 (2020) <http://dx.doi.org/10.1016/j.electacta.2020.137142>.
- [46] J. Huang, M. Papac, R. O'Hayre, Towards robust autonomous impedance spectroscopy analysis: A calibrated hierarchical Bayesian approach for electrochemical impedance spectroscopy (EIS) inversion, *Electrochim. Acta* 367 (2021) <http://dx.doi.org/10.1016/j.electacta.2020.137493>.